Most probable fission configurations and symmetric-asymmetric fission competition in Hg isotopes

Pooja Chauhan[1,2] Dalip Singh Verma[1†]

[1]Department of Physics and Astronomical Science, Central University of Himachal Pradesh, Dharamshala, District Kangra (H.P.)-176215 India
[2]Department of Physics, Panjab University, Chandigarh-160014, India

Abstract: The most probable fission fragment configurations (A_L,A_H), (Z_L,Z_H), and (N_L,N_H), together with the relative contributions of the symmetric and asymmetric fission channels, are systematically studied over a range of excitation energies for ^{178,180,182,183,184,190,192,194,195,196,198}Hg* isotopes using the dynamical cluster-decay model. The model uses updated bulk and neutron–proton asymmetry coefficients of the mass formula, adjusted to the AME2020 and/or FRDM(2012) mass evaluations, along with the temperature-dependent surface-energy coefficient and nuclear deformations. The calculations show a consistent preference for charge-asymmetric configurations near the deformed shell closures $(Z_L,Z_H)=(36,44)$ at lower excitation energies throughout the isotopic chain. The neutron partition (N_L,N_H) shows weaker isotopic dependence in the light fragment than in the heavy fragment; the calculated light-fragment neutron number remains near $N_L\approx 50$, while the heavy fragment accommodates a larger fraction of the isotopic neutron excess. For the lighter isotopes, $^{178-184}$Hg*, the asymmetric channel contribution dominates at low excitation energies and is associated with the deformed shell closures $(Z_L,Z_H)=(36,44)$. At higher excitation energies, the symmetric-fission channel contribution dominates and is associated with $(Z_L=Z_H=40)$. The transition toward predominantly symmetric fission occurs at an excitation energy of approximately 50 MeV. For the heavier isotopes, $^{190-198}$Hg*, the asymmetric fission channel contribution likewise decreases with excitation energy, while the symmetric fission channel contribution increases, resulting in a near balance between the two fission channels at higher excitation energies. The increase in the calculated symmetric-fission-channel cross section with excitation energy is consistent with the increasing trend observed in the available experimental cross sections.

Keywords: Asymmetric fission, light-fragment configurations, Hg isotopes, dynamical cluster-decay model, shell effects, symmetric--asymmetric fission-channel competition, excitation energy, sub-lead nuclei

DOI: **CSTR:**

CPC Accepted

I. INTRODUCTION

The study of nuclear fission dynamics in mercury isotopes has attracted considerable attention in recent years, particularly following the unexpected observation of asymmetric fission in the neutron-deficient nucleus ^{180}Hg* by Andreyev *et al.* [1]. This result was surprising because shell-effect considerations should favour a symmetric mass division into doubly magic ^{90}Zr fragments. The observed asymmetry therefore challenged the traditional view that fragment shell closures alone determine the most probable fission mode in this mass region. The observation was subsequently confirmed through a series of heavy-ion reaction experiments [2−4]. Consequently, extensive experimental [5−10] and theoretical [11−18] efforts have been carried out to understand the fission of Hg isotopes at different excitation energies. For example, asymmetric fission is observed at low excitation energy in the fission of various Hg nuclei: ^{182,195}Hg* [5], ^{180,190}Hg* [6], ^{182,184,192,196,198}Hg* [7], ^{178}Hg* [8], ^{192}Hg* [9], and ^{194}Hg* [10]. At higher excitation energy, the dominant asymmetric fission mode changes to a symmetric one; see, for example, the evolution of the fission mode with excitation energy in the fission of ^{180,182,183}Hg* [4], ^{180,190}Hg* [6], and ^{192}Hg* [9].

On the theoretical front, calculated mass-yield distributions for $^{174-188}$Hg were reported to vary with compound-nucleus neutron number and excitation energy in Ref. [11], using a Brownian Metropolis shape-motion treatment. A transition from asymmetric fission toward increasingly symmetric fission with increasing mass of the Hg compound nucleus was demonstrated in Refs. [12, 13], using nuclear density functional theory and potential-

Received 29 September 2026; Accepted 11 November 2026
† E-mail: dsverma@cuhimachal.ac.in (Corresponding author)
©2027 Chinese Physical Society and the Institute of High Energy Physics of the Chinese Academy of Sciences and the Institute of Modern Physics of the Chinese Academy of Sciences and IOP Publishing Ltd. All rights, including for text and data mining, AI training, and similar technologies, are reserved.

energy-surface calculations, and in Refs. [14, 15], [18], using an improved scission-point model. The transition from asymmetric to symmetric fission with excitation energy has been shown in Refs. [13] and [17] using calculations based on finite-temperature density functional theory and the general description of fission observables (GEF) model, respectively.

The observed asymmetric fission of Hg isotopes in most of the above-mentioned theoretical and experimental studies is attributed to the deformed shell closures associated with the nascent fragments at low excitation energies. For example, the most probable fragment configurations are due to deformed proton shell closures at $Z = 34, 36, 38, 42, 44$ and 46, and neutron shell closures at $N = 42$–46, as reported in the theoretical studies of Refs. [16–18], and at $(Z_L, Z_H = 36 \pm 2, 44 \pm 2$ for ^{180}Hg* [1]) and $Z = 36, 46$ in experimental studies [4, 7–10]. Other studies [19, 20] also show that shell stabilization associated with a deformed proton shell at $Z = 36$ plays a decisive role in generating asymmetric fission in neutron-deficient nuclei. The evolution of the fission mode with excitation energy occurs because the shell corrections and deformations vary with excitation energy [4, 6, 9, 13, 17].

Recently, the asymmetric fission of ^{180}Hg* and the transition from asymmetric to symmetric fission with excitation energy have been successfully explained by our research group using the DCM with an updated nuclear mass formula with refined bulk and neutron-proton asymmetry coefficients, as well as temperature-dependent surface-energy and deformation effects [21, 22]. Motivated by these developments, the present work systematically investigates the evolution of fragment mass distributions and the competition between symmetric and asymmetric fission in Hg isotopes with compound-nucleus neutron number and excitation energy within the framework of the DCM. The calculations at low excitation energy reveal that the proton number of the most probable light fragment varies only slightly ($Z_L \approx$ 35-37) across the isotopic chain, indicating a persistent preference for fragments around the deformed shell closures at $Z = 36$ and 44 (complementary binary fragments). Furthermore, the calculations show a distinct excitation-energy dependence for the fission of $^{178-184}$Hg* and $^{190-198}$Hg*. The lighter isotopes $^{178-184}$Hg* exhibit a pronounced transition from predominantly asymmetric fission at low excitation energies to increasing symmetric-fission contributions with increasing excitation energy, whereas in the heavier isotopes $^{190-198}$Hg*, the contributions of the asymmetric and symmetric channels become nearly balanced at higher excitation energies. The transition from the dominant asymmetric fission mode to the symmetric one occurs at $E^*_{CN} \approx$ 50 MeV, except for ^{178}Hg*, where the transition takes place at 35 MeV. The increase in the symmetric fission channel contribution with excitation energy follows the experimentally observed trend.

The methodology is presented in Section II, the results are discussed in Section III, and the conclusions are summarized in Section IV.

II. METHODOLOGY

The dynamical cluster-decay model (DCM) [23, 24], based on quantum-mechanical fragmentation theory [25–27], is formulated in terms of the collective coordinates of mass asymmetry, $\eta = (A_1 - A_2)/(A_1 + A_2)$, or charge asymmetry, $\eta_Z = (Z_1 - Z_2)/(Z_1 + Z_2)$, and the relative separation R. It also includes the deformation parameters $\beta_{\lambda i}$ ($\lambda = 2, 3,$ and 4 corresponding to quadrupole, octupole, and hexadecapole deformations, respectively), the orientation angles θ_i of the interacting fragments, and the angles α_i between the radius vector and the symmetry axis of the corresponding fragment. Here, $i = 1, 2$ denotes the heavy and light fragments, respectively. The η coordinate describes the nucleon partitioning or exchange between the outgoing fragments, whereas the R coordinate describes the transfer of kinetic energy from the incident channel to the total kinetic energy (TKE) and total excitation energy (TXE) of the outgoing channel. The formation of the binary fragments is treated as a preformation process, followed by their dynamical motion through the interaction barrier. Accordingly, the preformation probability P_0 is determined from the fragmentation potential in the η coordinate, while the barrier penetrability P is evaluated along the relative-separation coordinate R. The energy balance in the DCM is expressed as

$$E^*_{\rm CN} = E_{\rm cm} + Q_{\rm in} = |Q_{\rm out}(T)| + {\rm TKE}(T) + {\rm TXE}(T) \quad (1)$$

where $E^*_{\rm CN}$ is the excitation energy of the compound nucleus and $E_{\rm cm}$ is the center-of-mass energy of the incident channel. The quantities $Q_{\rm in}$ and $Q_{\rm out}(T)$ denote the Q-values of the incoming and outgoing channels, respectively, and are defined as $Q_{\rm in} = B_1(T = 0) + B_2(T = 0) - B_{CN}(T = 0)$ and $Q_{\rm out}(T) = B_{CN}(T) - B_1(T) - B_2(T)$, where $B_{\rm CN}$ and B_i ($i = 1, 2$) are the binding energies of the compound nucleus and the two fragments, respectively. Thus, the compound-nucleus excitation energy is distributed in the outgoing channel among the magnitude of the outgoing-channel Q-value, the total kinetic energy, and the total excitation energy of the fragments.

The fragment-production cross section in the DCM is expressed in terms of partial waves as

$$\sigma = \frac{\pi}{k^2} \sum_{\ell=0}^{\ell_{max}} (2\ell + 1) P_0 P; \quad k = \sqrt{\frac{2\mu E_{cm}}{\hbar^2}} \quad (2)$$

The preformation probability P_0 in Eq. 2 refers to the η motion, whereas the penetration probability P refers to

CPC Accepted

the R-motion of the fragments. $\mu = \frac{1}{4}mA_{CN}(1-\eta^2)$ represents the reduced mass, where $A_{CN}(=A_1+A_2)$ is the mass of the compound nucleus and m is the nucleon mass. The maximum angular momentum up to which the cross section is summed is denoted by ℓ_{max}. Here, ℓ_{max} is taken to be equal to the critical angular momentum, given by:

$$\ell_c = R_a\sqrt{2\mu\left[E_{cm}-V(R_a,\eta_{inc},\ell=0)\right]}/\hbar \tag{3}$$

Here, $V(R_a,\eta_{inc},\ell=0)$ denotes the entrance-channel interaction potential at the first turning point, R_a $(=X_1+X_2+\overline{\Delta R}$, where X_i represents the projection of the nuclear radius vector along the collision axis; see Fig. 1 of Ref. [21]). The term $\overline{\Delta R}$ denotes the internuclear surface separation. The preformation probability associated with the η-motion is obtained from the numerical solution of the stationary Schrödinger equation:

$$\left\{-\frac{\hbar^2}{2\sqrt{B_{\eta\eta}}}\frac{\partial}{\partial\eta}\frac{1}{\sqrt{B_{\eta\eta}}}\frac{\partial}{\partial\eta}+V\right\}\psi^{\nu}(\eta)=E^{\nu}\psi^{\nu}(\eta) \tag{4}$$

where $B_{\eta\eta}$ are the hydrodynamic masses from Ref. [28], and the T-dependent solutions are included as follows:

$$|\psi|^2=\sum_{\nu=0}^{\infty}|\psi^{\nu}|^2\exp\left(-\frac{E^{\nu}}{T}\right) \tag{5}$$

where $\nu=0,1,2,3,...$ labels the ground state $(\nu=0)$ and excited states $(\nu=1,2,3,...)$ of the η motion. The fragment preformation probability P_0 is

$$P_0(A_i)=|\psi(\eta(A_i))|^2\sqrt{B_{\eta\eta}}\left(\frac{2}{A_{CN}}\right) \tag{6}$$

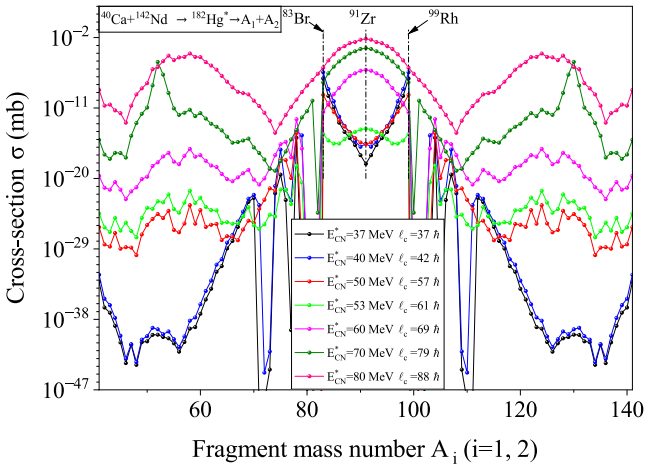

Fig. 1. (color online) Calculated cross section for ^{182}Hg* formed in the ^{40}Ca+^{142}Nd reaction [4] as a function of the fragment mass number A_i $(i=1,2)$ at excitation energies of 37–80 MeV.

where $|\psi(\eta(A_i))|^2$ is obtained from the stationary Schrödinger equation with the fragmentation potential V $[=V(R,\eta,\beta_{2i},\theta_i,\alpha_i,\ell,T)]$, evaluated at the fixed internuclear separation R $(=R_a)$. The fragmentation potential is calculated from the temperature-dependent mass excesses of the interacting fragments and their mutual interaction potentials, including the nuclear proximity, Coulomb, and centrifugal contributions, given as

$$V=\sum_{i=1}^{2}\left[\Delta M_i(A_i,Z_i,\beta_{2i},T)\right]+V_P(R,\eta,\beta_{2i},\theta_i,T) +V_C(R,\eta_Z,\beta_{2i},\alpha_i,T)+V_\ell(R,\eta,\beta_{2i},\alpha_i,\ell,T) \tag{7}$$

where $\Delta M_i(A_i,Z_i,\beta_{2i},T)$ denotes the temperature-dependent mass excess, a measure of the binding energy expressed as the sum of the liquid-drop energy V_{LDM} [29], including its temperature dependence from Ref. [30], and the shell-correction term δU [31], with its temperature dependence taken from Ref. [32]. The mass excess, calculated using new bulk and neutron–proton asymmetry coefficients in the nuclear shape-dependent mass-excess formula fitted to the recent mass-excess data reported in AME2020 [33] and/or FRDM(2012) [34], is taken from [35]. The temperature dependence of the quadrupole-deformation parameter $\beta_2(T)$ is taken from Ref. [21] and is given by:

$$\beta_2(T)=\begin{cases}\beta_2(T=0), & T=0\\ \beta_2(T=0)\left[1+\exp\left(\dfrac{T-a}{b}\right)\right]^{-1}, & T>0\end{cases} \tag{8}$$

where b is taken as $|\beta_2(T=0)|$, and a is set to 6.7 b. The temperature (T) of the compound nucleus corresponding to the excitation energy E^*_{CN} (both in MeV) is obtained as

$$E^*_{CN}=\left(\frac{A_{CN}}{9}\right)T^2-T \tag{9}$$

The nuclear proximity potential V_P is that of Blocki et al. [36] and is given by

$$V_P(R,\eta,\beta_{\lambda i},\theta_i,T)=4\pi\overline{R}(\eta,\beta_{\lambda i},T)b(T)\gamma(T) \times\Phi(s(R,\eta,\beta_{\lambda i},\theta_i,T)) \tag{10}$$

where $\overline{R}(\eta,\beta_{\lambda i},T)$ is the mean radius of curvature; see Ref. [37] for details. The temperature-dependent surface energy coefficient $\gamma(T)$ is taken from Ref. [38] and is given by

$$\gamma(T)=\gamma(1-0.07T)^2 \tag{11}$$

CPC Accepted

where $\gamma = 0.9517\left[1-1.7826I^2\right]$ MeV fm^{-2} is the surface energy coefficient of the Lysekil mass formula, $I=(N-Z)/A$, and N, Z, and A refer to the combined system of the two interacting nuclei. The universal function $\Phi(s)$ is

$$\Phi(s)=\begin{cases} -\frac{1}{2}(s-2.54)^2-0.0852(s-2.54)^3, & s\le 1.2511 \\ -3.437\exp(-s/0.75), & s\ge 1.2511 \end{cases}$$

where $s\,(=s_0/b)$ represents the minimum distance between the surfaces of the colliding nuclei per unit surface thickness, b. The temperature dependence in the universal function is introduced through the temperature-dependent quantities $s_0(T)$ and $b(T)(=0.99(1+0.009T^2))$ [39], both expressed in fm. The quantity $s_0(=R-X_1-X_2)$ is minimized with respect to the angle α_i. Here, $X_1\,(=R_1(\alpha_1,T)\cos(\theta_1-\alpha_1))$ and $X_2(=R_2(\alpha_2,T)\cos(\pi+\theta_2-\alpha_2))$ are the projections of the radius vector $R_i(\alpha_i,T)$ along the collision axis; see Fig. 1 of Ref. [21]. The Coulomb potential for a system of two deformed and oriented nuclei with atomic numbers Z_1 and Z_2 at a separation R(T) is [40]

$$\begin{aligned} V_C(R,\eta_Z,\beta_{\lambda i},\alpha_i,T) = {} & \frac{Z_1Z_2e^2}{R(T)}+\sum_{\lambda,i=1,2}\left(\frac{3Z_1Z_2e^2}{2\lambda+1}\right) \\ & \times\frac{R_i^{\lambda}(\alpha_i,T)}{R(T)^{\lambda+1}}Y_{\lambda}^{(0)}(\alpha_i) \\ & \times\left[\beta_{\lambda i}+\frac{4}{7}\beta_{\lambda i}^2Y_{\lambda}^{(0)}(\alpha_i)\right] \end{aligned} \tag{12}$$

where the summation is over the multipole orders λ and the interacting-nucleus index i, and $Y_{\lambda}^{(0)}(\alpha_i)$ is the spherical harmonic of order λ. The nuclear radius vector for multipole orders $\lambda=2,3,4,...$ is

$$R_i(\alpha_i,T)=R_{0i}(T)\left[1+\sum_{\lambda}\beta_{\lambda i}Y_{\lambda}^{(0)}(\alpha_i)\right] \tag{13}$$

The temperature dependence of the nuclear radius vector $R_i(\alpha_i)$ is introduced through the temperature-dependent effective sharp radius $R_{0i}(T)$ of Ref. [39] (in fm), given as

$$R_{0i}(T)=\left(1.28A_i^{\frac{1}{3}}-0.76+0.8A_i^{-\frac{1}{3}}\right)\left(1+0.0007T^2\right) \tag{14}$$

The centrifugal potential term is

$$V_{\ell}(R,\eta,\beta_{\lambda i},\alpha_i,\ell,T)=\frac{\ell(\ell+1)\hbar^2}{2I_s(T)} \tag{15}$$

where $I_s(T)=\mu R^2+\frac{2}{5}A_1mR_1^2(\alpha_1,T)+\frac{2}{5}A_2mR_2^2(\alpha_2,T)$ denotes the moment of inertia in the complete sticking limit. The fragment penetration probability P is given by the WKB integral as

$$P=\exp\left[-\frac{2}{\hbar}\int_{R_a}^{R_b}\sqrt{2\mu\left[V(R)-Q_{eff}\right]}dR\right] \tag{16}$$

where R_a and R_b are the first and second turning points along the penetration path through the potential $V(R)$, which is the sum of the nuclear, Coulomb, and centrifugal potentials. The potential $V(R_a)$ at R_a serves as the effective Q-value (Q_{eff}) for the decay of a hot compound nucleus at temperature T into two fragments observed in their ground states. For details, see Fig. 1 of Ref. [24].

III. RESULTS AND DISCUSSION

The most probable fission-channel configurations in the fission of ^{178,180,182,183,184,190,192,194,195,196,198}Hg* isotopes have been studied within the framework of the dynamical cluster-decay model. The fragments are assumed to be in the touching configuration ($\overline{\Delta R}=0$ fm) and aligned along their optimal hot orientations before the onset of penetration. The partial-wave cross section is summed over angular momenta up to the critical angular momentum determined from Eq. (3). The reactions forming different Hg isotopes, along with the other input parameters used in the calculations, are listed in Table 1.

A. Most probable fission-fragment configurations: Evolution with compound-nucleus mass

Fig. 1 shows the fission-fragment cross section as a function of fragment mass number for ^{182}Hg* at different excitation energies, illustrating the evolution of the mass distribution with increasing excitation energy. Although the figure covers a relatively broad range of fragment mass numbers, we restrict our discussion to the mass region $(A_{CN}/2)\pm 20$, which includes the most probable fission-fragment configurations considered in the present study. This choice is consistent with earlier studies [1, 2, 4, 21, 22], in which the symmetric and asymmetric fission peaks are found within the $(A_{CN}/2)\pm 20$ mass region.

Fig. 1 shows that the fission-fragment mass distribution is predominantly asymmetric at an excitation energy of 37 MeV, corresponding to the energy reported in Ref. [4]. At this excitation energy, the calculated fission cross section is summed over angular momenta up to the critical angular momentum ℓ_c (=37 $\hbar$). The asymmetric fission peaks are located at ^{83}Br + ^{99}Rh, corresponding to $Z_L=35$, $N_L=48$ and $Z_H=45$, $N_H=54$, respectively, and are associated with the deformed proton-shell regions near $Z_L=36$ and $Z_H=44$. This result agrees well with the experimental observations reported in Refs. [4, 7]. With increasing excitation energy, the asymmetric contribu-

CPC Accepted

Table 1. Heavy-ion reactions leading to the formation of various Hg isotopes, along with the corresponding incident center-of-mass energies E_{cm}, entrance-channel Q-values Q_{in}, compound-nucleus excitation energies $E^*_{CN}(= E_{cm} + Q_{in})$, and temperatures T (all in MeV), as well as the critical angular momenta ℓ_c (in $\hbar$).

Reaction	E_{cm} (MeV)	Q_{in} (MeV)	E^*_{CN} (MeV)	T (MeV)	ℓ_c ($\hbar$)	Ref.
$^{124}Xe + ^{54}Fe \rightarrow ^{178}Hg^*$	161.53	−127.53	34.0	1.34	54	[8]
$^{36}Ar + ^{144}Sm \rightarrow ^{180}Hg^*$	126.40	−91.49	34.9	1.34	46	[3]
	144.50	−91.49	53.0	1.65	67	
$^{40}Ca + ^{142}Nd \rightarrow ^{182}Hg^*$	133.11	−96.11	37.0	1.38	37	[4]
	148.11	−96.11	52.0	1.63	60	
	164.11	−96.11	68.0	1.86	77	
$^{40}Ca + ^{143}Nd \rightarrow ^{183}Hg^*$	134.32	−95.32	39.0	1.41	40	[4]
	150.33	−95.32	55.0	1.67	63	
	166.33	−95.32	71.0	1.89	80	
$^{40}Ca + ^{144}Nd \rightarrow ^{184}Hg^*$	136.76	−90.96	45.8	1.52	44	[7]
$^{36}Ar + ^{154}Sm \rightarrow ^{190}Hg^*$	127.86	−71.16	56.7	1.66	59	[3]
	146.46	−71.16	75.3	1.91	78	
$^{32}S + ^{160}Gd \rightarrow ^{192}Hg^*$	117.01	−62.80	54.2	1.62	64	[9]
	137.11	−62.80	74.3	1.89	74	
$^{12}C + ^{182}W \rightarrow ^{194}Hg^*$	77.75	−16.85	60.9	1.70	47	[10]
$^{13}C + ^{182}W \rightarrow ^{195}Hg^*$	55.31	−13.50	41.8	1.41	35	[5]
$^{12}C + ^{184}W \rightarrow ^{196}Hg^*$	55.95	−13.55	42.4	1.42	36	[7]
$^{12}C + ^{186}W \rightarrow ^{198}Hg^*$	54.38	−9.58	44.8	1.45	35	[7]

CPC Accepted

tion gradually decreases, whereas the symmetric component increases. Around $E^*_{CN} \approx 53$ MeV, the symmetric configuration becomes dominant and remains prominent at higher excitation energies. The symmetric fission peak is located at ^{91}Zr + ^{91}Zr, corresponding to $Z = 40$ and $N = 51$ in each fragment, and is associated with the spherical proton shell closure at $Z = 40$. Thus, with increasing excitation energy, the relative dominance shifts from deformation-based shell stabilization associated with the asymmetric configuration ^{83}Br + ^{99}Rh to stabilization associated with the spherical $Z = 40$ shell closure, thereby favouring the symmetric fission configuration ^{91}Zr + ^{91}Zr.

Fig. 2 compares the most probable fission-fragment partitions obtained for the fission of $^{178,180,182,183,184,190,192,194,195,196,198}Hg^*$ isotopes. The DCM calculations are performed using the input parameters with the lowest excitation energies listed in Table 1. The three panels show the corresponding fragment mass numbers (A_i), proton numbers (Z_i), and neutron numbers (N_i), respectively. Here, $i = L, H$ denotes the light and heavy fragments, respectively. This notation is adopted in place of the labels 1 and 2 used in the methodology section for the heavy and light fragments, respectively, to maintain consistency with the literature used for comparison.

Fig. 2 (a) shows that the most probable mass partitions are predominantly asymmetric. With increasing compound-nucleus mass (A_{CN}), the heavy-fragment mass (A_H) increases systematically, whereas the light-fragment mass (A_L) remains comparatively localized across the Hg isotopic chain. Thus, the increase in A_{CN} is accommodated predominantly by the heavy fragment rather than being distributed equally between the two fragments. The corresponding proton partitions shown in Fig. 2 (b) exhibit markedly different behavior. The most probable proton numbers remain nearly unchanged across the entire isotopic chain, with average values of $\overline{Z}_L = 35.6$ and $\overline{Z}_H = 44.4$, as indicated by the dot-dashed lines. Thus, despite the increase in A_{CN}, the most probable charge-asymmetric configuration remains localized near the $Z_L = 36$ and $Z_H = 44$ regions, corresponding approximately to the $Br - Kr$ and $Ru - Rh$ regions, respectively. This persistence of the proton partition indicates that the most probable asymmetric fission pathway is associated with a relatively stable charge configuration (36, 44). In contrast, Fig. 2 (c) shows a systematic increase in the neutron numbers of both fragments with increasing A_{CN}. The increase is more pronounced for the heavy fragment, consistent with the behavior observed in the mass partition. Thus, while the proton numbers of the most prob-

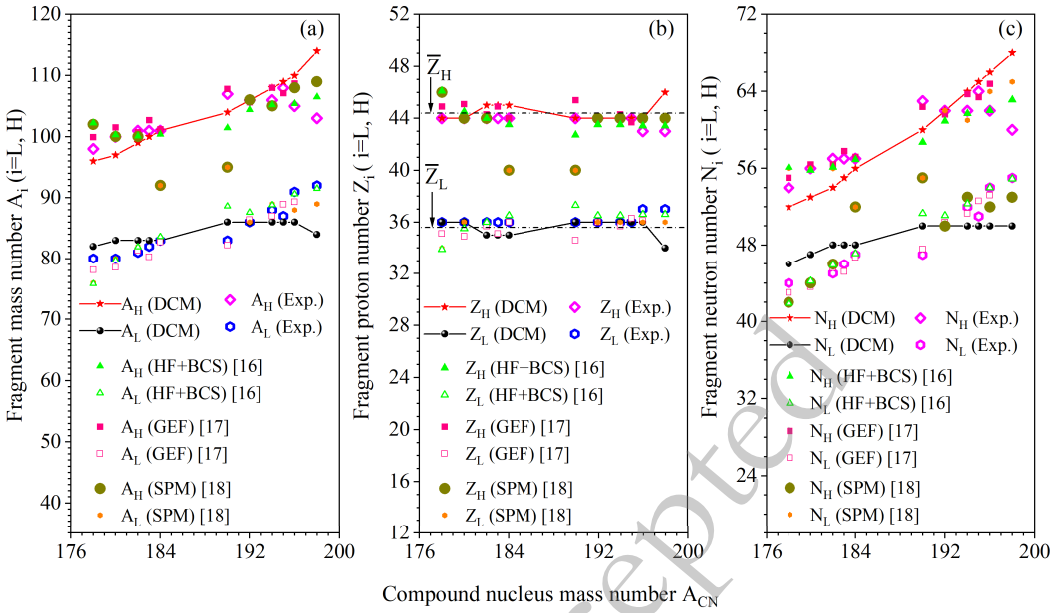

Fig. 2. (color online) Fission-fragment mass number A_i, proton number Z_i, and neutron number N_i for the most probable combination as functions of A_{CN}, obtained from (i) DCM, (ii) experimental data [3, 4, 7−10], and (iii) theoretical predictions based on the Hartree–Fock approach with BCS pairing correlations (HF+BCS) [16], the General Description of Fission observables (GEF) model [17], and the Scission-Point Model (SPM) [18].

CPC Accepted

able fragments remain nearly fixed, the additional neutrons introduced along the Hg isotopic chain are preferentially accommodated by the heavy fragment. The combined behavior of A_i, Z_i, and N_i therefore indicates that the evolution of the most probable mass partition is governed primarily by the redistribution of neutrons between the fragments, whereas the proton partition remains comparatively stable. The persistence of fragment proton numbers near $Z_L = 36$ and $Z_H = 44$ further indicates energetically favored proton configurations associated with the asymmetric fission pathway.

A comparison of the DCM results with the available experimental data [3, 4, 7−10] and with theoretical results from the GEF code [17], the scission-point model (SPM) [18], and the microscopic calculations of Scamps *et al.* using the Hartree-Fock approach with BCS pairing correlations (HF+BCS) [16] is also shown in Fig. 2. The DCM calculations show generally good agreement with the experimentally observed asymmetric fission behavior in terms of the most probable A_i, Z_i, and N_i partitions. A notable deviation occurs for ^{196,198}Hg*, for which the experimental data exhibit a relatively stronger symmetric-fission component, whereas the DCM calculations at $E^*_{CN} = 42.4$ MeV for ^{196}Hg* and 44.8 MeV for ^{198}Hg* still favor a predominantly asymmetric mass distribution. Comparison with the other theoretical approaches also shows reasonable consistency. An exception is found for ^{184}Hg* and ^{190}Hg*, for which the SPM calculations of Ref. [18] predict nearly symmetric fission, whereas both the experimental measurements and the present DCM calculations favor asymmetric fragment partitions. It is worth noting that the GEF calculations of Ref. [17] use the experimental excitation energies, whereas the SPM calculations correspond to excitation energies approximately 2 MeV above the fission barrier.

B. Evolution of Fission modes with Excitation Energy

Figs. 3(a−e) show the evolution of the most probable proton configurations (Z_L, Z_H) with excitation energy for the lighter isotopes ^{178,180,182,183,184}Hg*. At low excitation energies, the most probable configurations are predominantly asymmetric, with $Z_L = 35$–36 and $Z_H = 44$–45, corresponding to the deformed-shell-favoured light-fragment region near $Z_L = 36$. With increasing excitation energy, these isotopes tend toward symmetric charge partitions, with the most probable configurations approaching $Z_L = Z_H = 40$. The available experimental data, although limited to one or two excitation energies for some isotopes, are in reasonable agreement with the calculated proton configurations. This agreement supports the persistence of the asymmetric configurations associated with the deformed proton-shell region at the experimentally investigated low excitation energies. At higher excitation energies, the calculations indicate the dominance of configurations with spherical proton-shell closure at $Z_L = Z_H = 40$.

Figs. 3(f−j) show a more varied dependence on excitation energy for the heavier isotopes. For ^{190,192,194}Hg*, the most probable proton configurations evolve from $(Z_L, Z_H) \approx (36, 44)$ at lower excitation energies toward

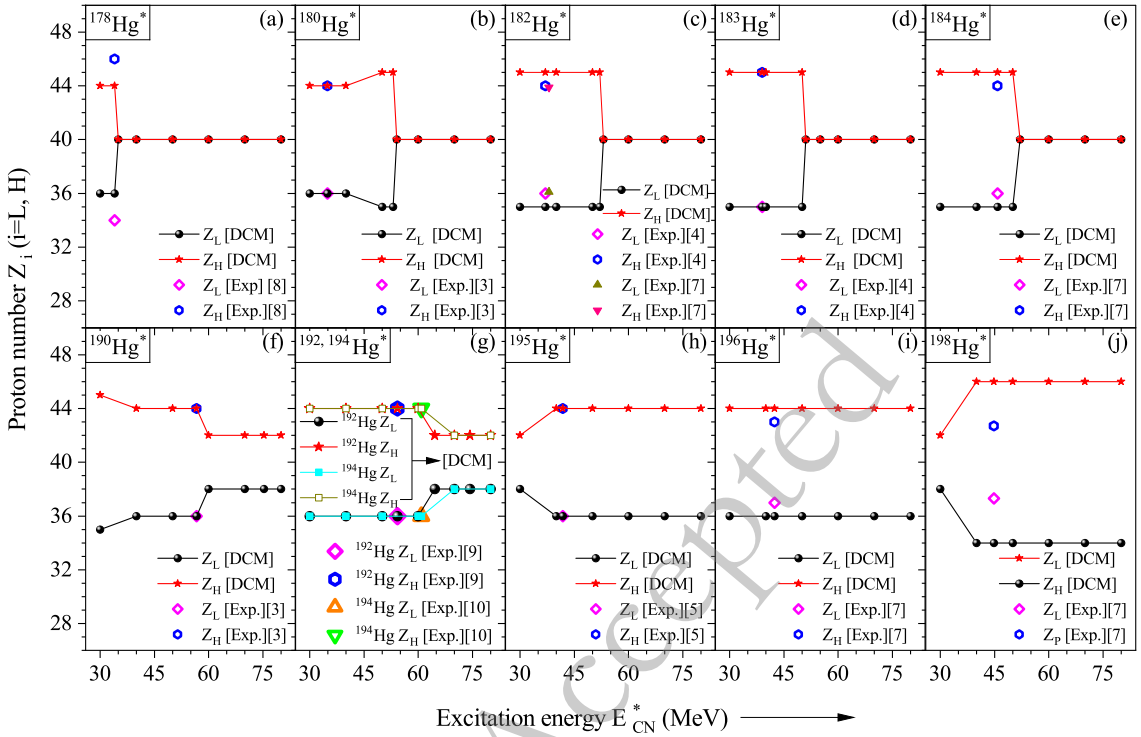

Fig. 3. (color online) Evolution with excitation energy of the proton configurations (Z_L,Z_H) of the most probable fission channel for the ^{178,180,182,183,184,190,192,194,195,196,198}Hg* isotopes, calculated within the DCM and compared with the available experimental data [3, 4, 7−10].

CPC Accepted

(38,42) at higher excitation energies. This gradual shift indicates increasing competition from less asymmetric configurations as excitation energy increases. Where available, the experimental results follow these calculated asymmetric charge configurations, while the calculations illustrate their evolution over a wider excitation-energy range than is currently accessible experimentally. In contrast, the most probable proton configurations of ^{195}Hg* and ^{196}Hg* remain concentrated near $(Z_L,Z_H)=(36,44)$ over most of the excitation-energy range considered, indicating that the asymmetric charge configuration remains comparatively robust. The behaviour of ^{198}Hg* is distinct: the most probable configuration is comparatively less asymmetric, $(Z_L,Z_H)=(38,42)$, at the lowest excitation energy, whereas at higher excitation energies, the calculation favours the more asymmetric partition (34,46). Thus, ^{198}Hg* does not exhibit a simple monotonic evolution toward symmetric charge division. Overall, the lighter Hg isotopes exhibit a systematic evolution from deformed-shell-favoured asymmetric configurations toward the symmetric configuration associated with the spherical $Z=40$ shell closure with increasing excitation energy, whereas the heavier isotopes show a more diverse excitation-energy dependence. The calculated proton partitions are generally consistent with the available experimental results, with a few exceptions.

Figs. 4 (a−e) show that, at low excitation energies, the most probable neutron-asymmetric configurations for the lighter isotopes ^{178,180,182,183,184}Hg* are $N_L\approx 46-48$ and $N_H\approx 54-56$. With increasing excitation energy, the most probable neutron numbers evolve toward more symmetric partitions with $N_L=N_H$, except for ^{183}Hg*, where $N_L\approx N_H$. The transition from asymmetric to symmetric configurations occurs within $E^*_{CN}\approx 40-60$ MeV, depending on the isotope, and coincides with the evolution of the corresponding proton configurations near the semi-magic proton number $Z=40$.

Figs. 4 (f−j) show that, in contrast to the lighter isotopes, the heavier isotopes ^{190,192,194,195,196,198}Hg* exhibit a comparatively stable light-fragment neutron number, with N_L remaining at 50 over most of the excitation-energy range. This indicates the persistence of the spherical neutron-shell closure at $N=50$ in the light fragment. The corresponding N_H values depend on the mass of the fissioning nucleus and generally increase with $A_{\rm CN}$, indicating that the additional neutrons along the isotopic chain are accommodated predominantly by the heavy fragment. Thus, the $N=50$ shell-stabilized light-fragment configuration remains robust with increasing excitation energy, in contrast to the more pronounced evolution toward symmetric neutron partitions observed for the lighter isotopes. This behavior is consistent with earlier studies of sub-lead fission [3, 4, 10, 17]. Overall, the lighter and heavier Hg isotopes exhibit distinctly different excitation-energy dependences in their most probable neutron configurations.

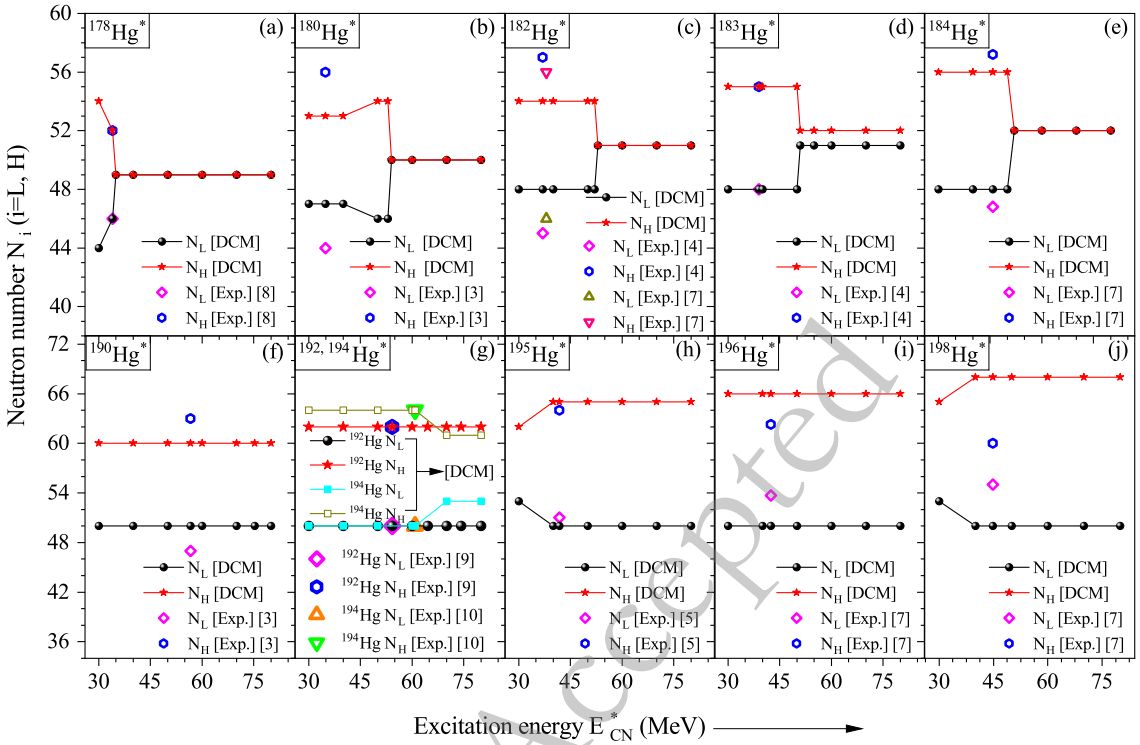

Fig. 4. (color online) As in Fig. 3, but showing the evolution of the most probable neutron configurations (N_L, N_H) as a function of excitation energy.

CPC Accepted

Figs. 5 (a–e) show that the asymmetric fission channel contribution dominates at low excitation energies for the lighter Hg isotopes: ^{178,180,182,183,184}Hg*. With increasing excitation energy, the asymmetric-fission channel contribution decreases, whereas the symmetric channel component increases, leading to a transition from predominantly asymmetric to predominantly symmetric fission. For ^{178}Hg*, this transition occurs abruptly around $E^*_{CN} \approx 33-35$ MeV, where the symmetric contribution rapidly rises to nearly 100% while the asymmetric component vanishes. A similar transition is obtained for ^{180}Hg* at the higher excitation energy of $E^*_{CN} \approx 52-55$ MeV. The isotopes ^{182,183,184}Hg* exhibit pronounced coexistence of symmetric and asymmetric fission channels over a narrow excitation-energy interval around $E^*_{CN} \approx 50-55$ MeV, where their contributions become comparable. This behaviour indicates direct competition between asymmetric configurations stabilised by deformed shell effects and more symmetric configurations associated with the spherical shell closure at $Z = 40$. The increase in the calculated symmetric-fission channel cross section with excitation energy is consistent with the increasing trend observed in the experimental cross sections for the symmetric-fission mode of ^{180}Hg*, ^{182}Hg*, and ^{183}Hg*.

Figs. 5 (f–j) show distinctly different behaviour for the heavier isotopes $^{190-198}$Hg*. The asymmetric-fission channel contribution decreases gradually with increasing excitation energy, whereas the symmetric component increases correspondingly. The contributions of the two fission channels become comparable at the highest excitation energies; however, the asymmetric-fission channel contribution remains dominant throughout. This indicates a gradual enhancement of the symmetric-fission channel contribution rather than the abrupt transition observed in the lighter isotopes. The available experimental data for the symmetric-fission mode of ^{190}Hg* and ^{192}Hg* lie close to the calculated values. It may be noted that the increase in the calculated symmetric-fission channel cross section with excitation energy follows the same trend as the experimental variation for the symmetric-fission mode; see Figs. 5 (b-d, f-g).

The contrasting behaviour of the lighter $^{178-184}$Hg* and heavier $^{190-198}$Hg* isotopes reflects the different responses of their most probable fragment configurations to increasing excitation energy. For the lighter isotopes, the most probable proton and neutron configurations evolve rapidly toward symmetric partitions between the two fission modes. In contrast, the heavier isotopes retain largely persistent shell-stabilized configurations, particularly those associated with $N_L \approx 50$, resulting in a more gradual evolution of the symmetric and asymmetric fission yields.

IV. CONCLUSIONS

The evolution of the most probable fragment config-

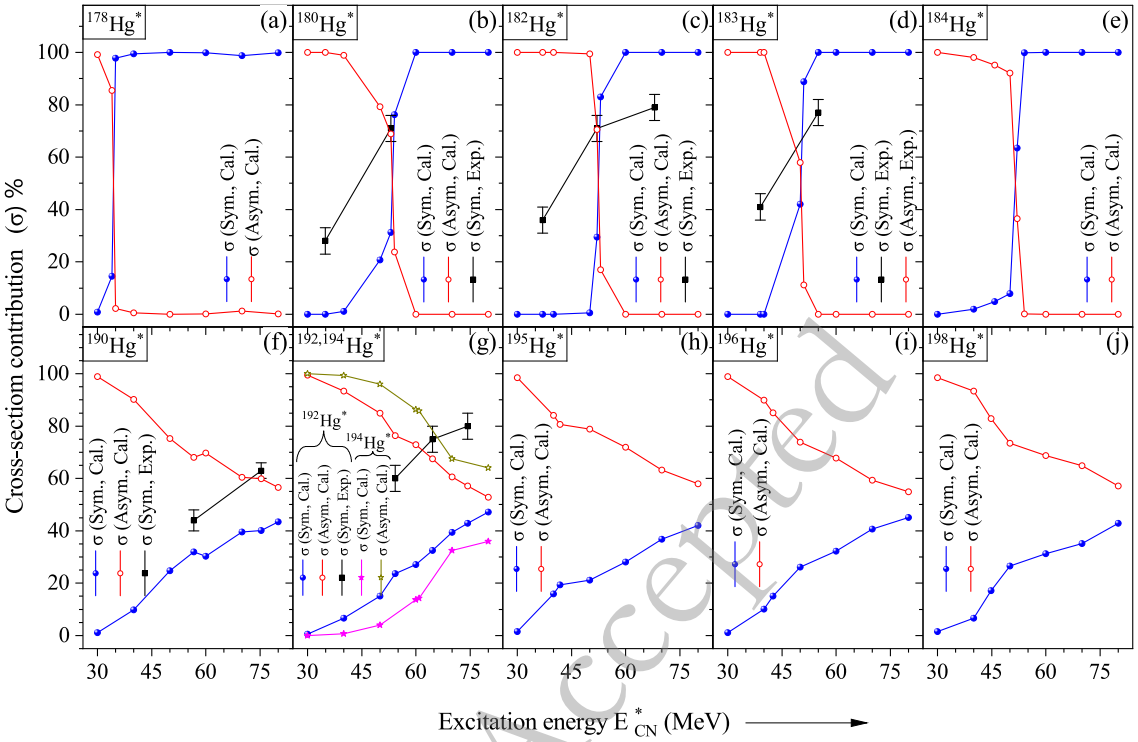

Fig. 5. (color online) Percentage contributions of the calculated symmetric σ(Sym., Cal.) and asymmetric σ(Asym., Cal.) fission channels as functions of the compound-nucleus excitation energy E^*_{CN} for the compound nuclei ^{178,180,182,183,184,190,192,194,195,196,198}Hg* at their respective critical angular momenta ℓ_c listed in Table 1. The available experimental yields, σ(Sym., Exp.) [3, 4, 9], are shown for comparison.

CPC Accepted

urations and the competition between symmetric and asymmetric fission channels in the $^{178-198}$Hg* isotopes have been investigated using the DCM with updated nuclear mass formulas that incorporate refined bulk and neutron–proton asymmetry coefficients, along with temperature-dependent surface-energy and deformation effects. The main conclusions of this study are as follows:

1. Across the isotopic chain, the most probable asymmetric fission-fragment configurations remain confined to a narrow region of the nuclear chart, with proton numbers $Z_L = 35-37$ and $Z_H = 43-45$, centred on the deformed shell closures at $Z = 36$ and 44.

2. The neutron content of the most probable fragments increases with the neutron number of the compound nucleus, whereas the isotopic dependence of the light-fragment neutron number is weaker than that of the heavy fragment. The persistence of configurations near $N_L \approx 50$ in several heavier Hg isotopes is consistent with enhanced stability in the $N = 50$ region.

3. The lighter isotopes $^{178-184}$Hg* exhibit a pronounced excitation-energy dependence: the asymmetric fission channel is dominant at low energies and is associated with deformed proton shell closures ($Z_L, Z_H \approx 36, 44$), whereas the symmetric fission channel dominates at higher excitation energies and is associated with proton shell closures ($Z_L = Z_H = 40$). By contrast, for the heavier isotopes $^{190-198}$Hg*, the dominant fission channel remains nearly independent of excitation energy, and N_L remains at 50 over most of the excitation-energy range.

4. For the lighter isotopes $^{178-184}$Hg*, the transition from the dominant asymmetric fission channel to the symmetric fission channel is abrupt and occurs at an excitation energy of approximately 50 MeV, except for ^{178}Hg*, for which the transition energy is nearly 35 MeV. For the heavier isotopes $^{190-198}$Hg*, strong competition between the symmetric and asymmetric fission channels is observed.

5. A distinct difference is observed in the excitation-energy dependence of fission-mode transitions between the lighter $^{178-184}$Hg* isotopes and the heavier $^{190-198}$Hg* isotopes.

ACKNOWLEDGMENTS

The authors thank the Central University of Himachal Pradesh for providing the necessary facilities to complete this work.

DECLARATIONS

The authors declare that they have no known competing financial interests or personal relationships that could be perceived to have influenced the work reported in this paper.

References

[1] A. N. Andreyev, J. Elseviers, M. Huyse *et al.*, Phys. Rev. Lett. **105**, 252502 (2010)
[2] K. Nishio, A. Andreyev, R. Chapman *et al.*, Phys. Lett. B **748**, 89 (2015)
[3] A. A. Bogachev, E. M. Kozulin, G. N. Knyazheva *et al.*, Phys. Rev. C **104**, 024623 (2021)
[4] E. Kozulin, G. Knyazheva, I. Itkis *et al.*, Phys. Rev. C **105**, 014607 (2022)
[5] E. Prasad, D. Hinde, K. Ramachandran *et al.*, Phys. Rev. C **91**, 064605 (2015)
[6] D. Kumar, E. Kozulin, M. Cheralu *et al.*, Phys. **84**, 1001 (2020)
[7] E. Prasad, D. Hinde, M. Dasgupta *et al.*, Phys. Lett. B **811**, 135941 (2020)
[8] A. Jhingan, C. Schmitt, A. Lemasson *et al.*, Phys. Rev. C **106**, 044607 (2022)
[9] R. Kumar, M. Maiti, A. Pal *et al.*, Phys. Rev. C **107**, 034614 (2023)
[10] K. Miernik, P. Garczyński, A. Korgul *et al.*, Phys. Rev. C **113**, 044624 (2026)
[11] P. Möller, J. Randrup, and A. J. Sierk, Phys. Rev. C **85**, 024306 (2012)
[12] M. Warda, A. Staszczak, and W. Nazarewicz, Phys. Rev. C **86**, 024601 (2012)
[13] J. McDonnell, W. Nazarewicz, J. Sheikh *et al.*, Phys. Rev. C **90**, 021302 (2014)
[14] A. Andreev, G. Adamian, and N. Antonenko, Phys. Rev. C **86**, 044315 (2012)
[15] A. Andreev, G. Adamian, N. Antonenko, and A. Andreyev, Phys. Rev. C **88**, 047604 (2013)
[16] G. Scamps and C. Simenel, Phys. Rev. C **100**, 041602 (2019)
[17] P. Kaur and M. Maiti, Nucl. Phys. A **1039**, 122727 (2023)
[18] D.-y. Huo, Z. Wei, K. Wu *et al.*, Eur. Phys. J. A **60**, 1 (2024)
[19] P. Morfouace, J. N. Wilson, D. Ramos *et al.*, Nature **641**, 339 (2025)
[20] V. Muddam, J. Buete, K. Cook *et al.*, EPJ Web Conf. **368**, 00022 (2026)
[21] D. S. Verma, P. Chauhan, A. S. Pawar, and Vivek, Nucl. Phys. A **1050**, 122926 (2024)
[22] D. S. Verma, P. Chauhan, and Vivek, Nucl. Phys. A **1055**, 123017 (2025)
[23] R. K. Gupta, R. Kumar, N. K. Dhiman *et al.*, Phys. Rev. C **68**, 014610 (2003)
[24] R. K. Gupta, M. Balasubramaniam, R. Kumar *et al.*, Phys. Rev. C **71**, 014601 (2005)
[25] J. Maruhn, W. Greiner, W. Scheid, Heavy Ion Collisions, vol. **397**, North-Holland, Amsterdam, (1980).
[26] R. K. Gupta, W. Scheid, and W. Greiner, Phys. Rev. Lett. **35**, 353 (1975)
[27] R. K. Gupta, M. Balasubramaniam, R. Kumar *et al.*, J. Phys. G: Nucl. Part. Phys. **31**, 631 (2005)
[28] H. Kroger and W. Scheid, J. Phys. G: Nucl. Part. Phys. **6**, L85 (1980)
[29] P. A. Seeger, Nucl. Phys. **25**, 1 (1961)
[30] N. J. Davidson, S. S. Hsiao, J. Markram *et al.*, Nucl. Phys. A **570**, 61c (1994)
[31] W. D. Myers and W. J. Swiatecki, Nucl. Phys. **81**, 1 (1966)
[32] A. S. Jensen, J. Damgaard, Nuclear Phys. A **203**, 578 (1973)
[33] M. Wang, W. J. Huang, F. G. Kondev *et al.*, Chin. Phys. C **45**, 3 (2021)
[34] P. Möller, A. J. Sierk, T. Ichikawa, H. Sagawa, At. Data Nucl. Data Tables **109**, 1 (2016)
[35] D. S. Verma, Vivek, and Kushmakshi, At. Data Nucl. Data Tables **155**, 101619 (2024)
[36] J. Blocki, J. Randrup, W. Swiatecki, and C. Tsang, Ann. Phys. **105**, 427 (1977)
[37] R. K. Gupta, N. Singh, and M. Manhas, Phys. Rev. C **70**, 034608 (2004)
[38] A. Daei-Ataollah, O. N. Ghodsi, and M. Mahdavi, Phys. Rev. C **97**, 054621 (2018)
[39] G. Royer and J. Mignen, J. Phys. G: Nucl. Part. Phys. **18**, 1781 (1992)
[40] C. Wong, Phys. Rev. Lett. **31**, 766 (1973)

CPC Accepted